# Structure Dependence of the Intermediate-Frequency Raman Modes in Isolated Single-Walled Carbon Nanotubes

Jinyong Wang, Juan Yang,* Daqi Zhang, and Yan Li*

Beijing National Laboratory for Molecular Sciences, State Key Laboratory of Rare Earth Materials Chemistry and Applications, Key Laboratory for the Physics and Chemistry of Nanodevices, College of Chemistry and Molecular Engineering, Peking University, Beijing 100871, China

**ABSTRACT:** Resonance Raman spectra in the intermediate-frequency mode (IFM) region have been studied for isolated single-walled carbon nanotubes (SWNTs) at the single-nanotube level. The SWNT samples with diameter in the range of 0.8−2.0 nm are first grown on quartz substrate and then transferred to silicon substrate by nanotransfer printing technique. A specific linear relation of $\omega_{RBM} = 222.0/d_t + 8.0$ is found to best suit for our transferred isolated SWNTs. By measuring more than 80 isolated SWNTs with 36 different assigned chiralities using five different excitation lasers, the dependence of the nondispersive out-of-plane transverse optical (oTO) and the dispersive IFM⁻ and IFM⁺ features on the nanotube structure has been determined. It is found that the oTO, IFM⁻, and IFM⁺ frequencies decrease slightly, decrease significantly, and increase slightly with decreasing nanotube diameter, respectively. The appearance of the oTO band is indifferent to SWNT chirality or type, while the IFM⁻ feature can only be observed in metallic or MOD1 semiconducting nanotubes with small chiral angles. The IFM⁻ feature in resonance Raman spectra thus offers a method to distinguish small $\theta$ nanotubes from large $\theta$ nanotubes and distinguish MOD1 semiconducting nanotubes from MOD2 semiconducting nanotubes.
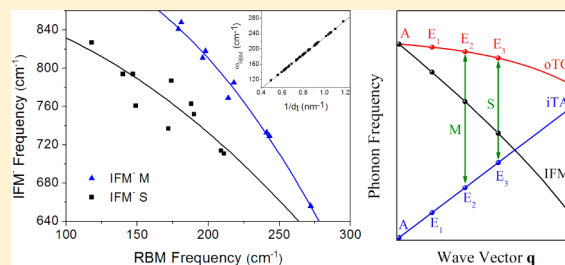
## INTRODUCTION

Resonance Raman spectroscopy (RRS) has been widely used to investigate the electronic and phonon structures of single-walled carbon nanotubes (SWNTs).[1−5] In addition to the well-studied first-order Raman features of the radial breathing mode (RBM, 100−400 cm⁻¹)[6−8] and the tangential G-band (~1590 cm⁻¹),[9,10] as well as the defect-related one-phonon double-resonance D-band (~1350 cm⁻¹)[11−13] and their overtones or combinational modes, several weak Raman features can also be observed in the intermediate-frequency region between 600 and 1100 cm⁻¹ for SWNT samples, namely the intermediate-frequency modes (IFM).[14−16] In the IFM region for bulk SWNT samples, both dispersive and nondispersive features with respect to the excitation laser energy ($E_{laser}$) have been observed in previous papers by Fantini et al.[17,18] A broad band at about 860 cm⁻¹ for electric-arc sample and about 845 cm⁻¹ for HiPco sample has been reported to be nondispersive and assigned as a Raman active feature related to the out-of-plane transverse optical (oTO) phonon branch in two-dimensional (2D) graphite. A steplike dispersion behavior has been observed for peaks above and below the nondispersive oTO peak, referred to as IFM⁺ and IFM⁻, respectively, and has been explained by a Raman process involving in the optical absorption/emission in the $E_{33}^{S}$ and $E_{44}^{S}$ energy range for semiconducting nanotubes and in the $E_{11}^{M-}$ and $E_{11}^{M+}$ energy range for metallic nanotubes.[17,18] A later study has found a new class of IFM also showing a steplike dispersive behavior in the spectral range of 380−650 cm⁻¹ and this has been associated with the $E_{11}^{S}$ and $E_{22}^{S}$ optical transitions of the semiconducting nanotubes in bundled HiPco samples.[19]

Due to the much weaker Raman intensity (1 order of magnitude less intense) than the RBM or G band, the IFM features were only studied in a small number of previous works,[17−25] all of which were carried out with bulk SWNT samples consisting of nanotube bundles with various (n,m). Except for one special case in which Fantini et al.[21] reported the simultaneously observed RBM, oTO, and IFM⁻ features for only one isolated SWNT grown across opened slits of a Si₃N₄ membrane, no other experimental data for the IFM features are observed and analyzed at the single-nanotube level yet. There are two main disadvantages in studying the IFM features and the related electronic and phonon structures with bulk SWNT bundles: First, the Raman signal of bulk SWNT sample comes from various (n,m) species and is only an averaged result of the mixture, which makes it difficult to analyze the spectral data with respect to individual nanotube chirality or type. Second, the interaction between SWNTs in bundles will possibly shift the frequency and change the intensity of the resonance Raman bands, introducing significant uncertainty in the obtained spectroscopic data. Therefore, it is important to study the IFM features of SWNTs at the single-nanotube level in order to better explore and understand the intrinsic electronic and phonon structures.

In the present work, horizontally aligned SWNT arrays are first grown on quartz substrate and then transferred to $SiO_x$/Si substrate by spin-coating poly(methyl methacrylate) (PMMA). The so-made isolated SWNTs on SiOx/Si substrate show a dilute density of ~0.6 SWNT/$\mu m^2$ and are used for resonance Raman measurement in both RBM and IFM regions under five different excitation laser energies. More than 80 isolated SWNTs with 36 different assigned chiralities show simultaneous RBM and IFM features, and these data are used for analysis. The nanotube diameters are obtained from the RBM frequencies by a linear relation $\omega_{RBM} = 222.0/d_t + 8.0$, which we believe is the best suitable relation for our transferred isolated SWNTs on $SiO_x$/Si substrate. Both the nondispersive oTO and the dispersive $IFM^-$ and $IFM^+$ features are analyzed with respect to individual nanotube structure. This is the first systematic work in which the IFM features of isolated SWNTs are studied at the single-nanotube level.

### ■ EXPERIMENTAL SECTION

**2.1. Sample Preparation and Transferring.** The horizontally aligned SWNT arrays were grown on single crystal quartz substrate (ST-cut, Hoffman Materials Inc.) using Fe nanoparticles as catalysts and ethanol as the carbon source.[26,27] A 1.0 mM $FeCl_3$/ethanol solution was used to deposit catalyst onto the quartz substrate. The growth was performed in a 1 in. Lindberg/blue tube furnace. The quartz substrate with deposited Fe catalyst precursors was first calcined in air at 700 °C for 5 min, then heated up to 900 °C in an argon flow of 400 sccm and reduced in 100 sccm hydrogen flow for 5 min. The chemical vapor disposition (CVD) growth of SWNTs was then carried out with a flow of 100 sccm hydrogen through an ethanol bubbler for 15 min. The substrate was cooled to room-temperature in argon flow. The strong interaction between the quartz lattice and the SWNTs guides the alignment of SWNTs on the surface of the substrate and prevents nanotube bundles from being formed.

The horizontally aligned SWNT arrays grown on quartz substrate were then transferred to SiOx/Si substrate with the nanotransfer printing technique.[28,29] By spin-coating 8% PMMA (Alfa Aesar, $M_w$ 350 000) anisole solution at 6000 rpm for 30 s on the quartz substrate with grown SWNT arrays, followed by baking at 110 °C for 30 min, the PMMA-SWNTs thin film can be peeled off from the quartz substrate by immersing it into a 1 mM KOH solution at 110 °C for 30 min. The peeled-off film was rinsed in ultrapure nanowater and then attached to a clean SiOx/Si substrate for baking at 110 °C for 30 min. Finally, PMMA was removed by dissolving in acetone for 30 min, and the transferred isolated nanotube arrays on SiOx/Si substrate were rinsed again in ultrapure nanowater.

For comparison purposes, a bulk SWNT sample was also prepared by an electric-arc method using a Ni/Y alloy as the catalyst and a graphite rod as the carbon source. The details for preparation and purification of the bulk electric-arc sample can be found elsewhere.[30]

**2.2. Characterization.** The Raman spectra of isolated SWNTs on SiOx/Si substrate were collected using two Raman systems: a Jobin Yvon LabRam HR 800 spectrometer with excitation laser lines of 488 nm (2.54 eV), 514 nm (2.41 eV), and 785 nm (1.58 eV), and a Jobin Yvon LabRam ARAMIS spectrometer with excitation laser lines of 532 nm (2.33 eV) and 633 nm (1.96 eV). The Raman spectra were taken in a backscattering configuration by a microscope using a 100× objective with laser focal spot of ~1 $\mu m^2$ and a charge coupled

device (CCD) detector. All laser power on SiOx/Si substrate was attenuated to be less than 1 mW to avoid heating effects. Due to the very weak intensity of the IFM features, integration time of 5 min was typically used in the Raman experiments.

The scanning electron microscopy (SEM) measurements were carried out on a Hitachi S4800 at an acceleration voltage of 1 kV.

### ■ RESULTS AND DISCUSSION

For comparison purposes, the resonance Raman spectra of the IFM features in the spectral region of 600−1100 $cm^{-1}$ for the bulk electric-arc SWNT sample excited at $E_{laser}$ of 2.54, 2.41, and 1.96 eV, respectively, are plotted in Figure 1. It can be seen
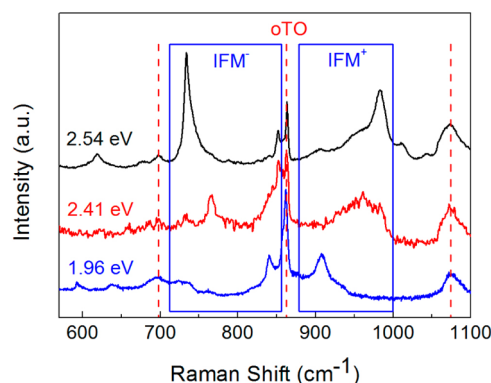


**Figure 1.** Resonance Raman spectra of the IFM features for the electric-arc sample excited at laser energies of 2.54, 2,41, and 1.96 eV. Red dashed lines indicate three nondispersive features at about 695, 860, and 1075 $cm^{-1}$. Blue solid rectangles indicate dispersive features of $IFM^-$ and $IFM^+$ at 710−850 $cm^{-1}$ and 880−1050 $cm^{-1}$, respectively.

from the spectra that the three peaks at about 695, 860, and 1075 $cm^{-1}$, indicated by the red dashed lines, do not shift with respect to $E_{laser}$ and are nondispersive. The dispersive features in the spectral regions of 710−850 $cm^{-1}$ and 880−1000 $cm^{-1}$, indicated by the blue solid rectangles, correspond to $IFM^-$ and $IFM^+$, respectively. The $IFM^-$ exhibits negative dispersion, whereas the $IFM^+$ shows positive dispersion with respect to $E_{laser}$. These data are in good agreement with previously reported IFM features for the electric-arc sample.[18] In this paper, we will mainly focus on the oTO, $IFM^-$, and $IFM^+$ features for isolated SWNTs.

Figure 2a shows the SEM image of the horizontally aligned SWNT arrays transferred to SiOx/Si substrate from quartz substrate with the nanotransfer printing technique.[28,29] The sample distributes a dilute density of ~0.6 SWNT/$\mu m^2$, which is important to ensure that both the RBM and IFM features observed at the same laser spot (~1 $\mu m^2$) come from the same isolated SWNT. The so-made isolated SWNTs have typical diameters ranging from 0.8 to 2.0 nm, obtained from the RBM frequency measurements.

As is well discussed, 2D graphene possesses an IR-active mode at about 868 $cm^{-1}$ arising from the oTO phonon mode. Theoretical studies predict a first-order Raman active peak at about 860 $cm^{-1}$ when the 2D graphene sheet rolls up to form a nanotube,[31,32] and this peak is indeed observed in the Raman spectra of SWNTs at the single-nanotube level. The oTO phonon mode in 2D graphene originates from the opposite out-of-plane vibration of the neighboring carbon atoms in the direction perpendicular to the graphene layer. When 2D
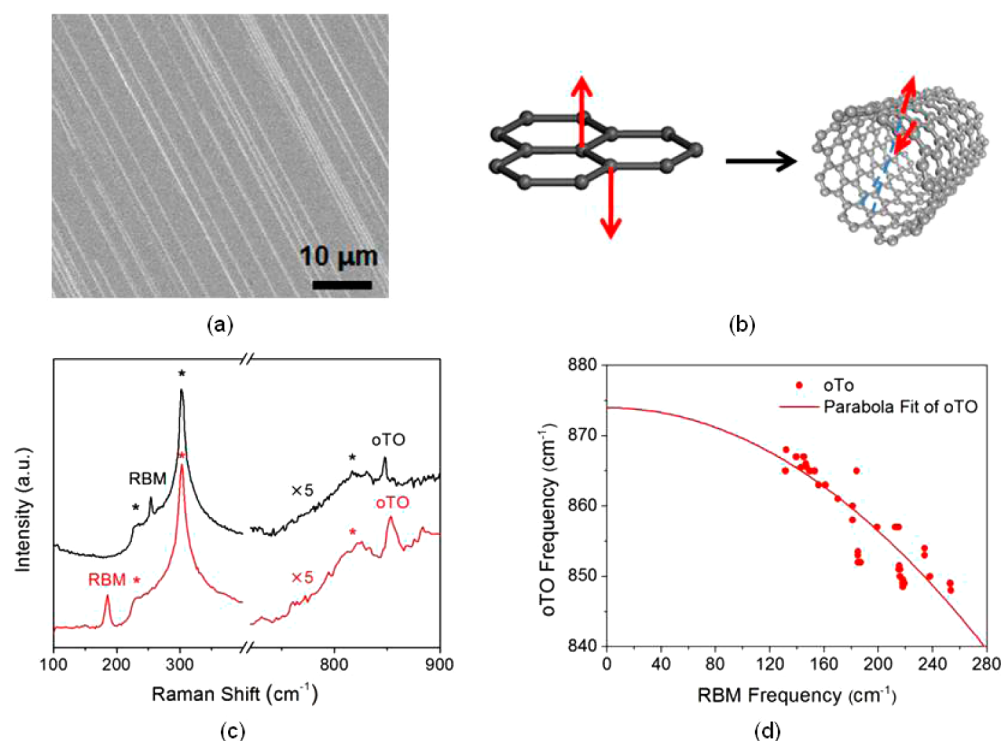
**Figure 2.** (a) SEM image of the horizontally aligned SWNT arrays transferred to SiOx/Si substrate from quartz substrate with the nanotransfer printing technique. The sample distributes an average density of ∼0.6 SWNT/$\mu m^2$. The scale bar is 10 $\mu$m. (b) Schematic diagram of the oTO phonon motion in graphene and SWNT. (c) The RBM and oTO Raman bands of two isolated SWNTs with different tube diameters on SiOx/Si substrate excited by 1.96 eV laser. The bands indicated by * are Raman signals arising from the SiOx/Si substrate. The spectra are normalized with respect to the 303 cm$^{-1}$ silicon band. (d) Observed oTO frequencies for 40 isolated SWNTs with 20 different assigned chiralities excited by five different lasers with respect to the observed RBM frequencies and the parabolic fit of the data points.

**Table 1. (n,m) Assignments of Isolated SWNTs with Observable oTO Features**

| $\omega_{RBM}$ (cm$^{-1}$) | $\omega_{oTO}$ (cm$^{-1}$) | $E_{Laser}$ (eV) | (n,m) | MOD (2n+m,3) | $d_t$ (nm) | $\theta$ | calc. $\omega_{RBM}$ (cm$^{-1}$) | $\Delta\omega_{RBM}$ (cm$^{-1}$) |
|---|---|---|---|---|---|---|---|---|
| 132 | 868 | 2.33 | (17,9) | 1 | 1.790 | 19.9 | 132.0 | 0.0 |
| 140 | 867 | 2.33 | (21,1) | 1 | 1.685 | 2.3 | 139.8 | −0.2 |
| 144 | 866 | 2.33 | (13,11) | 1 | 1.629 | 27.2 | 144.3 | 0.3 |
| 145 | 867 | 2.41 | (17,6) | 1 | 1.618 | 14.6 | 145.2 | 0.2 |
| 147 | 865 | 2.33 | (18,4) | 1 | 1.589 | 9.8 | 147.7 | 0.7 |
| 153 | 865 | 2.33 | (15,7) | 1 | 1.524 | 18.1 | 153.7 | 0.7 |
| 156 | 863 | 2.33 | (13,9) | 2 | 1.500 | 24.0 | 156.0 | 0.0 |
| 161 | 863 | 2.41 | (18,1) | 1 | 1.450 | 2.7 | 161.1 | 0.1 |
| 170 | 861 | 2.54 | (12,8) | 2 | 1.365 | 23.4 | 170.6 | 0.6 |
| 180 | 859 | 1.96 | (11,8) | 0 | 1.294 | 24.8 | 179.6 | −0.4 |
| 184 | 865 | 2.33 | (15,2) | 2 | 1.260 | 6.2 | 184.2 | 0.2 |
| 185 | 853 | 1.96 | (16,0) | 2 | 1.253 | 0 | 185.2 | 0.2 |
| 187 | 852 | 1.96 | (12,6) | 0 | 1.243 | 19.1 | 186.6 | −0.4 |
| 199 | 857 | 2.33 | (11,6) | 1 | 1.169 | 20.4 | 197.9 | −1.1 |
| 213 | 857 | 1.58 | (9,7) | 1 | 1.088 | 25.9 | 212.0 | −1.0 |
| 215 | 851 | 2.33 | (12,3) | 0 | 1.076 | 10.9 | 214.3 | −0.7 |
| 218 | 849 | 2.33 | (13,1) | 0 | 1.059 | 3.7 | 217.6 | −0.4 |
| 234 | 853 | 1.58 | (12,1) | 1 | 0.981 | 4.0 | 234.3 | 0.3 |
| 238 | 850 | 1.58 | (9,5) | 2 | 0.962 | 20.6 | 238.8 | 0.8 |
| 253 | 849 | 1.96 | (11,1) | 2 | 0.903 | 4.3 | 253.8 | 0.8 |

graphene rolls up to form a nanotube, it corresponds to the motion of the neighboring carbon atoms vibrating oppositely in the radial direction, as illustrated in Figure 2b. Therefore, the oTO mode is predicted to be diameter dependent, with increasing frequency when the tube diameter $d_t$ increases.[32] Figure 2c shows the RBM and oTO Raman bands of two isolated SWNTs with different tube diameters on SiOx/Si

substrate excited by 1.96 eV laser. The bands indicated by * are Raman signals arising from the SiOx/Si substrate. The spectra are normalized with respect to the 303 cm$^{-1}$ silicon band. As can be seen, the oTO band gives much weaker intensity than the RBM band, which makes it very difficult to observe at the single-nanotube level. In Figure 2c, the nanotube with higher RBM frequency exhibits slightly lower oTO frequency. Figure
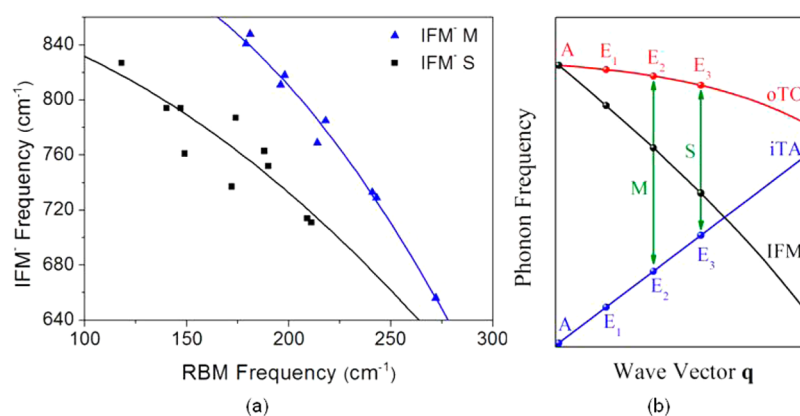
**Figure 3.** (a) Observed IFM⁻ frequencies of metallic (blue triangle) and semiconducting (black square) SWNTs with respect to the observed RBM frequencies. For clarity purposes, data points corresponding to the same assigned chirality are not displayed. (b) Schematic diagram of the phonon dispersion relations of oTO (red curve), iTA (blue curve), and their difference IFM⁻ (black curve) with respect to the phonon wave vector **q**.

**Table 2. (n,m) Assignments of Isolated SWNTs with Observable IFM⁻ Features**

| $\omega_{RBM}$ (cm⁻¹) | $\omega_{IMF-}$ (cm⁻¹) | $E_{Laser}$ (eV) | (n,m) | MOD (2n+m,3) | $d_t$ (nm) | $\theta$ | calc. $\omega_{RBM}$ (cm⁻¹) | $\Delta\omega_{RBM}$ (cm⁻¹) |
|---|---|---|---|---|---|---|---|---|
| 178 | 841 | 1.96 | (15,3) | 0 | 1.308 | 8.9 | 177.7 | −0.3 |
| 180 | 848 | 1.96 | (16,1) | 0 | 1.294 | 3.0 | 179.6 | −0.4 |
| 196 | 811 | 1.96 | (14,2) | 0 | 1.182 | 6.6 | 195.8 | −0.2 |
| 198 | 818 | 1.96 | (15,0) | 0 | 1.174 | 0 | 197.1 | −0.9 |
| 214 | 769 | 1.96 | (12,3) | 0 | 1.076 | 10.9 | 214.3 | 0.3 |
| 218 | 785 | 2.33 | (13,1) | 0 | 1.059 | 3.7 | 217.6 | −0.4 |
| 241 | 733 | 2.33 | (11,2) | 0 | 0.949 | 8.2 | 241.9 | 0.9 |
| 243 | 729 | 2.33 | (12,0) | 0 | 0.939 | 0 | 244.4 | 1.4 |
| 272 | 656 | 2.33 | (9,3) | 0 | 0.847 | 13.9 | 270.1 | −1.9 |
| 118 | 827 | 2.54 | (26,0) | 1 | 2.036 | 0 | 117.0 | −1.0 |
| 140 | 794 | 2.33 | (21,1) | 1 | 1.685 | 2.3 | 139.8 | −0.2 |
| 149 | 794 | 2.33 | (19,2) | 1 | 1.572 | 4.9 | 149.2 | 0.2 |
| 150 | 761 | 2.33 | (20,0) | 1 | 1.566 | 0 | 149.8 | −0.2 |
| 172 | 737 | 2.54 | (15,4) | 1 | 1.358 | 11.5 | 171.5 | −0.5 |
| 174 | 787 | 2.33 | (17,0) | 1 | 1.331 | 0 | 174.8 | 0.8 |
| 188 | 763 | 2.41 | (14,3) | 1 | 1.230 | 9.5 | 188.5 | 0.5 |
| 190 | 752 | 2.41 | (15,1) | 1 | 1.215 | 3.2 | 190.7 | 0.7 |
| 209 | 714 | 2.54 | (13,2) | 1 | 1.104 | 7.1 | 209.1 | 0.1 |
| 211 | 711 | 2.41 | (14,0) | 1 | 1.096 | 0 | 210.6 | −0.4 |

2d plots the observed oTO frequencies for 40 isolated SWNTs with 20 different assigned chiralities excited by five different $E_{laser}$ with respect to their observed RBM frequencies. The (n,m) assignments for the isolated SWNTs are made based on the resonance condition of $E_{laser}$ and $E_{ii}$ of the corresponding nanotubes, as well as the linear relation of $\omega_{RBM}$ and $1/d_t$ which will be further discussed in detail later. Since $\omega_{RBM}$ is inversely proportional to $d_t$, the results in Figure 2d suggest that the oTO mode is diameter dependent, and $\omega_{oTO}$ is positively related to $d_t$, in good accordance with the theoretical predictions.[32] A parabolic fit of the data points in Figure 2d gives an oTO frequency of 874 cm⁻¹ at $\omega_{RBM} = 0$, where $d_t \rightarrow \infty$ and corresponds to a 2D graphene sheet with a predicted oTO frequency of 868 cm⁻¹.

In the resonance Raman experiments in this work, the polarization of the incident laser is set to be parallel to the axis of the SWNT arrays. Only phonons with A symmetry can be observed according to the Raman selection rules.[3] The oTO phonon mode shows similar dispersion relation as the LO phonon mode in 2D graphene, the equi-energy contours of both exhibiting circular shape around the Γ point in the Brillouin zone. It becomes a maximum in phonon density of

state (DOS) at the Γ point in the Brillouin zone for the oTO phonon, and this maximum is indifferent to (n,m) when 2D graphene rolls up to form a nanotube. Therefore, the oTO band can be observed regardless of the SWNT (n,m) species or type as long as the resonance condition is met, i.e., $E_{laser}$ is within the resonance window of $E_{ii}$ to give a measurable Raman intensity. The (n,m) assignments of isolated SWNTs with observable oTO feature are summarized in Table 1. The oTO feature for SWNTs with various chiral angle and type, including both metallic MOD(2n+m,3) = 0 and semiconducting MOD(2n+m,3) = 1 or 2, hereafter referred to as MOD1 or MOD2, respectively, are indeed observed experimentally at the single-nanotube level.

The dispersive features of IFM⁻ and IFM⁺ are assigned as the combination of two phonons originated from the zone-folding procedure of the oTO and in-plane transverse acoustic (iTA) phonon branches in 2D graphene, the frequencies of which are given by

$$\omega_{IFM}^{+} = \omega_{oTO} + \omega_{iTA}$$

$$\omega_{IFM}^{-} = \omega_{oTO} - \omega_{iTA}$$

respectively. According to the phonon dispersion relation of 2D graphene around the $\Gamma$ point, oTO phonon frequency exhibits a relatively weak negative dispersion (a parabolic type), whereas iTA phonon frequency shows a strong positive dispersion (a linear type) along the nanotube $\mathbf{K}_1$ direction. By creation of both oTO and iTA phonons, the summation band IFM$^+$ thus exhibits relatively weak positive dispersion behavior. Additionally, by creation of an oTO phonon and annihilation of an iTA phonon, the difference band IFM$^-$ shows a relatively stronger negative dispersion.

Figure 3a plots the observed IFM$^-$ frequencies of both metallic and semiconducting isolated SWNTs at the single-nanotube level with respect to their observed RBM frequencies. For clarity purposes, extra data points corresponding to the same assigned chirality are not displayed. These data and the corresponding $(n,m)$ assignments are summarized in Table 2. It can be clearly seen from Figure 3a that for both metallic and semiconducting SWNTs, the IFM$^-$ frequencies decrease with increasing RBM frequencies, or with decreasing tube diameter $d_t$. The IFM$^-$ frequency for metallic nanotubes are higher than that for semiconducting nanotubes when the tube diameter $d_t$ is comparable.

In the model proposed by Fantini et al.,[17] the IFM features for metallic nanotubes originate from phonon modes with $E_2$ symmetry ($\mu_{phonon} = 2$), while the IFM features for semiconducting nanotubes are from that with $E_3$ symmetry ($\mu_{phonon} = 3$) in order to meet angular momentum conservation. Due to Raman selection rules, $E_3$ symmetry modes are not allowed in a first-order Raman scattering and can only be mediated by a second-order scattering process involving two $E_3$ phonons, for example, the combination of the oTO and iTA phonons. Figure 3b shows a schematic diagram of the phonon dispersion relations of oTO (red curve), iTA (blue curve), and their difference IFM$^-$ (black curve) with respect to the phonon wave vector $\mathbf{q}$. $A, E_1, E_2, E_3$, and so on are the corresponding phonon symmetries for the cutting lines with $\mu = 0,1,2,3,...$ The distance between the neighboring cutting lines, $|\mathbf{K}_1| = 2/d_t$, is inversely proportional to the tube diameter $d_t$. On one hand, when $d_t$ decreases, the distance between the neighboring cutting lines will increase, and the cutting lines with $E_2$ or $E_3$ symmetry will move further away from the $\Gamma$ point. Since the phonon frequency of the difference band IFM$^-$ exhibits a strong negative dispersion along the $\mathbf{K}_1$ direction, the IFM$^-$ frequency will decrease with decreasing $d_t$ for both metallic and semiconducting nanotubes. On the other hand, for nanotubes with comparable $d_t$, the distance between the neighboring cutting lines are close. As the $E_3$ symmetry phonon branch is further away from the $\Gamma$ point than the $E_2$ symmetry phonon branch, semiconducting nanotubes are suppose to give lower IFM$^-$ frequency than the metallic nanotube with comparable $d_t$. This well explains the observed diameter and type-dependent IFM$^-$ variation in Figure 3a.

In a first-order resonance Raman scattering process, the energy of either the incident phonon or the scattered phonon should match with the transition energy $E_{ii}$ between the van Hove singularities (vHSs) in the joint density of state (JDOS). The IFM$^-$ is a double-resonance Raman process that involves in an additional resonant electronic vHS state $E_{i'i'}$, to which the excited electron at $E_{ii}$ is scattered. In this work, the diameter of the isolated SWNTs is in the range of 0.8−2.0 nm, and the five different $E_{laser}$ values used are between 1.58 and 2.54 eV. The double-resonance phonon scattering process will mainly happen between $E_{33}^S$ and $E_{44}^S$ for semiconducting nanotubes

and between $E_{11}^{M-}$ and $E_{11}^{M+}$ for metallic nanotubes. Since the IFM$^-$ phonon energy ($\sim$0.1 eV) is much smaller compared to the electronic energies, the resonance is dominant only when the transition energies of $E_{ii}$ and $E_{i'i'}$ are very close to each other so that they can be connected by the IFM$^-$ phonon scattering. The energy difference between $E_{11}^{M-}$ and $E_{11}^{M+}$ for metallic nanotubes is well spaced to match with the IFM$^-$ phonon energy. However, the $E_{33}^S$ and $E_{44}^S$ energies are close enough only for MOD1 semiconducting nanotubes. The MOD2 semiconducting nanotubes exhibit spread-out family behavior in $E_{33}^S$ and $E_{44}^S$ energies, and their difference is too large to be connected by an IFM$^-$ phonon.

In a one-dimensional (1D) SWNT, both linear momentum conservation along the tube axis and angular momentum conservation around the tube axis are required to meet in order for an process to become Raman active. The linear momentum conservation requirement gives rise to $|\mathbf{q}_{phonon}| = |\mathbf{k}_f - \mathbf{k}_i|$, where $\mathbf{q}_{phonon}$ is the phonon wave vector along the tube axis and $\mathbf{k}_f$ and $\mathbf{k}_i$ denote the electronic wave vectors for the final and initial electronic states, respectively. In our case, $|\mathbf{q}_{phonon}| = |\mathbf{k}_4 - \mathbf{k}_3|$ for semiconducting nanotubes and $|\mathbf{q}_{phonon}| = |\mathbf{k}_{1+} - \mathbf{k}_{1-}|$ for metallic nanotubes, where $\mathbf{k}_4, \mathbf{k}_3, \mathbf{k}_{1+}, \mathbf{k}_{1-}$ represent the electronic wave vectors for $E_{44}^S, E_{33}^S, E_{11}^{M+}$, and $E_{11}^{M-}$, respectively. Because the phonon DOS is maximized at the $\Gamma$ point where $\mathbf{q}_{phonon} \rightarrow 0$, only electronic states with wave vectors $|\mathbf{k}_f - \mathbf{k}_i| \rightarrow 0$ can be best connected by the phonons at the phonon vHSs. According to the geometric structure of nanotubes, $\mathbf{k}_4 = \mathbf{k}_3$ happens only for $(n,0)$ zigzag semiconducting SWNTs, and $\mathbf{k}_{1+} = \mathbf{k}_{1-}$ happens for both $(n,0)$ zigzag and $(n,n)$ armchair metallic nanotubes, considering that the $E_{11}^{M+}$ and $E_{11}^{M-}$ are degenerate for $(n,n)$ nanotubes. However, since the $(n,n)$ nanotubes do not meet the condition of double-resonant electronic states connected by the IFM$^-$ phonon scattering, $|\mathbf{q}_{phonon}| = |\mathbf{k}_f - \mathbf{k}_i| \rightarrow 0$ is best satisfied for nanotubes with chiral angle $\theta \rightarrow 0$, or near-zigzag SWNTs. Therefore, due to the double-resonance condition constrain as well as the linear momentum conservation requirement, the IFM features can only be observed in metallic and MOD1 semiconducting nanotubes with chiral angle $\theta \rightarrow 0$.

In this work, the isolated SWNTs were first grown on a quartz substrate, then transferred onto SiOx/Si substrate using the PMMA peel-off method. Since PMMA coating and dissolution were involved in the sample preparation steps, the interaction between the so-made SWNTs and the surrounding environment might be different than that in directly grown SWNTs on either quartz or silicon substrates. The previously reported linear relations of $\omega_{RBM} = 227.0/d_t + 0.3$ for SWNTs on quartz substrate[6] and $\omega_{RBM} = 248/d_t$ for SWNTs on silicon substrate[7] were not suitable in our case. A specific linear relation between $\omega_{RBM}$ and $d_t$ that is suitable for our transferred isolated SWNTs need to be derived in order to make correct assignments and for further analysis.

This is done based on the IFM$^-$ data for metallic nanotubes. It can be found in Figure 3a that the IFM$^-$ data points for metallic nanotubes exhibit a steplike behavior. For example, the IFM$^-$ features can only be observed for SWNTs with $\omega_{RBM}$ close to 180, 198, 218, and 243 cm$^{-1}$. This steplike behavior was also observed previously in bulk SWNT samples with respect to $E_{laser}$. It can be associated with the different metallic nanotube families, which is in resonance with the corresponding $E_{laser}$. As the linear momentum conservation requirement allows only for nanotubes with $\theta \rightarrow 0$, the $\omega_{RBM}$ at 180, 198, 218, and 243 cm$^{-1}$ can be assigned to (16,1), (15,0), (13,1),

and (12,0), respectively, each possessing the smallest $\theta$ in the corresponding $2n+m$ families. The other closely spaced data points at 178, 196, 214, and 241 cm$^{-1}$ are assigned to (15,3), (14,2), (12,3), and (11,2), respectively, and each gives the second lowest $\theta$ in the corresponding $2n+m$ families. A linear relation of $\omega_{RBM} = 222.0/d_t + 8.0$ can be derived from those $(n,m)$ assignments. By using this linear relation to calculate $d_t$ from all observed $\omega_{RBM}$, and by applying the resonance condition between $E_{ii}$ and $E_{laser}$, the $(n,m)$ values for all isolated SWNTs are assigned. The difference between the calculated and observed RBM frequencies are within $\pm2$ cm$^{-1}$ for all 36 distinct chiralities, and are within $\pm1$ cm$^{-1}$ for 34 chiralities. Figure 4 plots all 36 observed $\omega_{RBM}$ and the linear fit with respect to $1/d_t$ of the assigned $(n,m)$. The fitting is excellent with an $R^2$ of 0.9997.
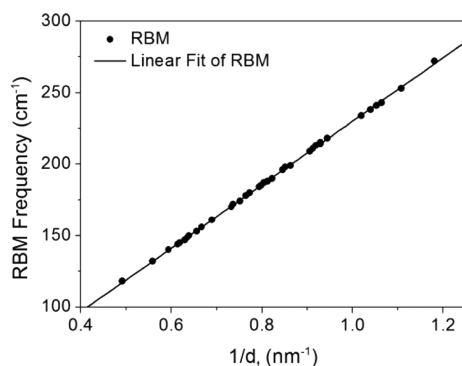


**Figure 4.** Linear fit of RBM frequencies with respect to $1/d_t$ for 36 distinct chiralities. The fitting function is $\omega_{RBM} = 222.0/d_t + 8.0$.

In addition to the excellent linearity, the $(n,m)$ assignments of IFM$^-$ for semiconducting nanotubes agree very well with the previously discussed double-resonance condition constrain and linear momentum conservation requirement, i.e., IFM$^-$ features are only observed for MOD1 semiconducting nanotubes with chiral angle $\theta \to 0$. Generally, the assigned $(n,m)$ in Table 2, for which the IFM$^-$ features are observed experimentally, are all with $\theta$ less than 15°, while that in Table 1, for which the oTO features are observed experimentally, corresponds to various $\theta$ values. The IFM$^-$ feature in resonance Raman spectra thus offers a method to distinguish small $\theta$ nanotubes from large $\theta$ nanotubes and distinguish MOD1 semiconducting nanotubes from MOD2 semiconducting nanotubes.

Figure 5a shows the observed IFM$^+$ frequencies of the isolated SWNTs at the single-nanotube level with respect to their observed RBM frequencies. Due to the extremely weak intensity, only 4 data points are observed. From the limited number of data points, it can only be concluded that the IFM$^+$ frequencies increase with increasing RBM frequencies, or with decreasing tube diameter $d_t$. For SWNTs with observed RBM frequencies in the range of 120−260 cm$^{-1}$, the difference in IFM$^+$ frequencies is only about 30 cm$^{-1}$, while that in IFM$^-$ frequencies is about 150 cm$^{-1}$, which demonstrate that the IFM$^+$ is less dispersive than IFM$^-$ with respect to tube diameter $d_t$. This can be explained by Figure 5b, which illustrates the schematic diagram of the phonon dispersion relations of oTO (red curve), iTA (blue curve) and their summation IFM$^+$ (black curve) with respect to the phonon wave vector $\mathbf{q}$. Since the IFM$^+$ phonon frequency exhibits a relatively weak positive dispersion along the $\mathbf{K}_1$ direction, when $d_t$ decreases all cutting lines will move further away from the $\Gamma$ point, resulting in increased IFM$^+$ frequency.

## ■ CONCLUSION

In this paper, the IFM features of isolated SWNTs in the spectral range of 600−1100 cm$^{-1}$ are studied by RRS at the single-nanotube level. Three types of features are discussed and analyzed: First, the nondispersive peak at about 860 cm$^{-1}$ is assigned to the oTO phonon mode, and it is found that $\omega_{oTO}$ is positively related to $d_t$ and that the appearance of the oTO band is indifferent to SWNT $(n,m)$ species or type. Second, the strong negative dispersive IFM$^-$ feature is assigned to the difference band of oTO and iTA phonon modes. The $\omega_{IFM-}$ increases with increasing $d_t$, and $\omega_{IFM-}$ for metallic nanotubes is higher than that for semiconducting nanotubes when $d_t$ is comparable. IFM$^-$ features can only be observed in metallic and MOD1 semiconducting nanotubes with small chiral angles. Third, the weak positive dispersive IFM$^+$ feature is assigned to the summation band of oTO and iTA phonon modes. The $\omega_{IFM+}$ decreases with increasing $d_t$.

## ■ AUTHOR INFORMATION

**Corresponding Author**
*E-mail: yang_juan@pku.edu.cn (J.Y.); yanli@pku.edu.cn (Y.L.). Tel: +86-10-62755357. Fax: +86-10-62755357.
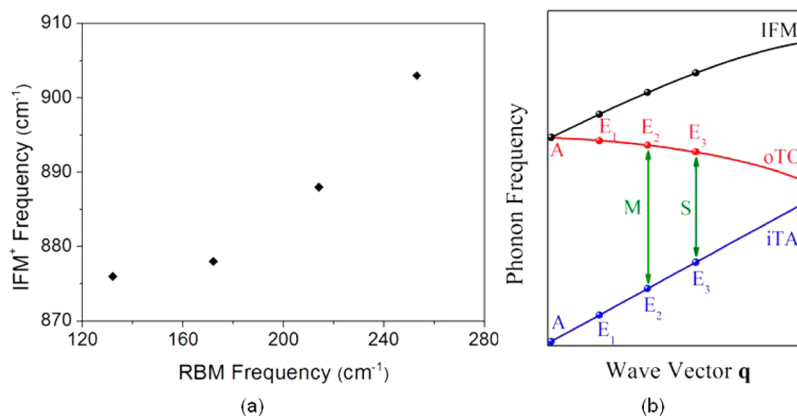


**Figure 5.** (a) Observed IFM$^+$ frequencies plotted with respect to the observed RBM frequencies. (b) Schematic diagram of the phonon dispersion relations of oTO (red curve), iTA (blue curve), and their summation IFM$^+$ (black curve) with respect to the phonon wave vector $\mathbf{q}$.

■ **REFERENCES**

(1) Kastner, J.; Pichler, T.; Kuzmany, H.; Curran, S.; Blau, W.; Weldon, D. N.; Delamesiere, M.; Draper, S.; Zandbergen, H. *Chem. Phys. Lett.* **1994**, *221*, 53−58.

(2) Dresselhaus, M. S.; Dresselhaus, G.; Jorio, A.; Souza, A. G.; Pimenta, M. A.; Saito, R. *Acc. Chem. Res.* **2002**, *35*, 1070−1078.

(3) Dresselhaus, M. S.; Dresselhaus, G.; Saito, R.; Jorio, A. *Phys. Rep.* **2005**, *409*, 47−99.

(4) Dresselhaus, M. S.; Dresselhaus, G.; Jorio, A. *J. Phys. Chem. C* **2007**, *111*, 17887−17893.

(5) Rao, A. M.; Bandow, S.; Richter, E.; Eklund, P. C. *Thin Solid Films* **1998**, *331*, 141−147.

(6) Araujo, P. T.; Maciel, I. O.; Pesce, P. B. C.; Pimenta, M. A.; Doorn, S. K.; Qian, H.; Hartschuh, A.; Steiner, M.; Grigorian, L.; Hata, K.; et al. *Phys. Rev. B* **2008**, *77*, 241403.

(7) Jorio, A.; Saito, R.; Hafner, J. H.; Lieber, C. M.; Hunter, M.; McClure, T.; Dresselhaus, G.; Dresselhaus, M. S. *Phys. Rev. Lett.* **2001**, *86*, 1118−1121.

(8) Maultzsch, J.; Telg, H.; Reich, S.; Thomsen, C. *Phys. Rev. B* **2005**, *72*, 205438.

(9) Saito, R.; Jorio, A.; Hafner, J. H.; Lieber, C. M.; Hunter, M.; McClure, T.; Dresselhaus, G.; Dresselhaus, M. S. *Phys. Rev. B* **2001**, *64*, 085312.

(10) Jorio, A.; Souza, A. G.; Dresselhaus, G.; Dresselhaus, M. S.; Swan, A. K.; Unlu, M. S.; Goldberg, B. B.; Pimenta, M. A.; Hafner, J. H.; Lieber, C. M.; et al. *Phys. Rev. B* **2002**, *65*, 155412.

(11) Thomsen, C.; Reich, S. *Phys. Rev. Lett.* **2000**, *85*, 5214−5217.

(12) Saito, R.; Gruneis, A.; Samsonidze, G. G.; Brar, V. W.; Dresselhaus, G.; Dresselhaus, M. S.; Jorio, A.; Cancado, L. G.; Fantini, C.; Pimenta, M. A.; et al. *New J. Phys.* **2003**, *5*, 157.

(13) Pimenta, M. A.; Jorio, A.; Brown, S. D. M.; Souza Filho, A. G.; Dresselhaus, G.; Hafner, J. H.; Lieber, C. M.; Saito, R.; Dresselhaus, M. S. *Phys. Rev. B* **2001**, *64*, 041401.

(14) Rao, A. M.; Richter, E.; Bandow, S.; Chase, B.; Eklund, P. C.; Williams, K. A.; Fang, S.; Subbaswamy, K. R.; Menon, M.; Thess, A.; et al. *Science* **1997**, *275*, 187−191.

(15) Saito, R.; Takeya, T.; Kimura, T.; Dresselhaus, G.; Dresselhaus, M. S. *Phys. Rev. B* **1999**, *59*, 2388−2392.

(16) Rahmani, A.; Sauvajol, J. L.; Rols, S.; Benoit, C. *Phys. Rev. B* **2002**, *66*, 125404.

(17) Fantini, C.; Jorio, A.; Souza, M.; Ladeira, L. O.; Souza Filho, A. G.; Saito, R.; Samsonidze, G. G.; Dresselhaus, G.; Dresselhaus, M. S.; Pimenta, M. A. *Phys. Rev. Lett.* **2004**, *93*, 087401.

(18) Fantini, C.; Jorio, A.; Souza, M.; Saito, R.; Samsonidze, G. G.; Dresselhaus, M. S.; Pimenta, M. A. *Phys. Rev. B* **2005**, *72*, 085446.

(19) Luo, Z. T.; Papadimitrakopoulos, F.; Doorn, S. K. *Phys. Rev. B* **2007**, *75*, 205438.

(20) Alvarez, L.; Righi, A.; Sols, S.; Anglaret, E.; Sauvajol, J. L. *Chem. Phys. Lett.* **2000**, *320*, 441−447.

(21) Fantini, C.; Jorio, A.; Souza, M.; Saito, R.; Samsonidze, G. G.; Dresselhaus, M. S.; Pimenta, M. A. *AIP Conf. Proc.* **2005**, *786*, 178−181.

(22) Kalbac, M.; Kavan, L.; Zukalova, M.; Dunsch, L. *Phys. Status Solidi B* **2006**, *243*, 3134−3137.

(23) Doorn, S. K.; Luo, Z. T.; Papadimitrakopoulos, F. *Phys. Status Solidi B* **2007**, *244*, 3992−3997.

(24) Popov, V. N.; Lambin, P. *Phys. Status Solidi B* **2010**, *247*, 892−895.

(25) Singh, D. K.; Iyer, P. K.; Giri, P. K. *J. Appl. Phys.* **2012**, *111*, 064304.

(26) Kocabas, C.; Hur, S.; Gaur, A.; Meitl, M. A.; Shim, M.; Rogers, J. A. *Small* **2005**, *1*, 1110−1116.

(27) Li, Y.; Cui, R.; Ding, L.; Liu, Y.; Zhou, W.; Zhang, Y.; Jin, Z.; Peng, F.; Liu, J. *Adv. Mater.* **2010**, *22*, 1508−1515.

(28) Jiao, L. Y.; Fan, B.; Xian, X. J.; Wu, Z. Y.; Zhang, J.; Liu, Z. F. *J. Am. Chem. Soc.* **2008**, *130*, 12612−12613.

(29) Liu, Z. F.; Jiao, L. Y.; Yao, Y. G.; Xian, X. J.; Zhang, J. *Adv. Mater.* **2010**, *22*, 2285−2310.

(30) Li, H. J.; Feng, L.; Guan, L. H.; Shi, Z. J.; Gu, Z. N. *Solid State Commun.* **2004**, *132*, 219−224.

(31) Eklund, P. C.; Holden, J. M.; Jishi, R. A. *Carbon* **1995**, *33*, 959−972.

(32) Dubay, O.; Kresse, G. *Phys. Rev. B* **2003**, *67*, 035401.